AGU PUBLICATIONS

Water Resources Research

RESEARCH ARTICLE
10.1002/2015WR018057

Influence of vertical and lateral heat transfer on permafrost thaw, peatland landscape transition, and groundwater flow

Barret L. Kurylyk[1], Masaki Hayashi[1], William L. Quinton[2], Jeffrey M. McKenzie[3], and Clifford I. Voss[4]

[1]Department of Geoscience, University of Calgary, Calgary, Alberta, Canada, [2]Cold Regions Research Centre, Wilfrid Laurier University, Waterloo, Ontario, Canada, [3]Earth and Planetary Sciences, McGill University, Montreal, Quebec, Canada, [4]National Research Program, U. S. Geological Survey, Menlo Park, California, USA

Abstract Recent climate change has reduced the spatial extent and thickness of permafrost in many discontinuous permafrost regions. Rapid permafrost thaw is producing distinct landscape changes in the Taiga Plains of the Northwest Territories, Canada. As permafrost bodies underlying forested peat plateaus shrink, the landscape slowly transitions into unforested wetlands. The expansion of wetlands has enhanced the hydrologic connectivity of many watersheds via new surface and near-surface flow paths, and increased streamflow has been observed. Furthermore, the decrease in forested peat plateaus results in a net loss of boreal forest and associated ecosystems. This study investigates fundamental processes that contribute to permafrost thaw by comparing observed and simulated thaw development and landscape transition of a peat plateau-wetland complex in the Northwest Territories, Canada from 1970 to 2012. Measured climate data are first used to drive surface energy balance simulations for the wetland and peat plateau. Near-surface soil temperatures simulated in the surface energy balance model are then applied as the upper boundary condition to a three-dimensional model of subsurface water flow and coupled energy transport with freeze-thaw. Simulation results demonstrate that lateral heat transfer, which is not considered in many permafrost models, can influence permafrost thaw rates. Furthermore, the simulations indicate that landscape evolution arising from permafrost thaw acts as a positive feedback mechanism that increases the energy absorbed at the land surface and produces additional permafrost thaw. The modeling results also demonstrate that flow rates in local groundwater flow systems may be enhanced by the degradation of isolated permafrost bodies.

Key Points:
- Observed permafrost thaw rates are compared to results from a 3-D groundwater flow and heat transfer model
- Lateral heat flow can accelerate discontinuous permafrost thaw and land cover change in peatlands
- Degradation of discontinuous permafrost enhances local groundwater flow

Supporting Information:
- Supporting Information S1

Correspondence to:
B. L. Kurylyk,
barret.kurylyk@ucalgary.ca

Citation:
Kurylyk, B. L., M. Hayashi, W. L. Quinton, J. M. McKenzie, and C. I. Voss (2016), Influence of vertical and lateral heat transfer on permafrost thaw, peatland landscape transition, and groundwater flow, *Water Resour. Res.*, *52*, 1286–1305, doi:10.1002/2015WR018057.

Received 7 SEP 2015
Accepted 24 JAN 2016
Accepted article online 28 JAN 2016
Published online 26 FEB 2016

1. Introduction

Subsurface thermal and hydrologic regimes are interrelated in cold regions because frozen and unfrozen soils store and transmit water differently and because subsurface heat transfer is influenced by moisture contents and fluxes [*Woo*, 2012; *Kurylyk et al*., 2014a]. Permafrost and seasonal pore ice reduce soil permeability and restrict shallow subsurface flow to the upper thawed zone (active layer) during the summer months [*Stähli*, 2005; *Watanabe and Flury*, 2008]. During the summer season, the location of the soil thawing front in permafrost regions controls the timing and magnitude of subsurface runoff and streamflow [*Metcalfe and Buttle*, 1999; *Quinton and Marsh*, 1999; *Carey and Woo*, 2005]. The distribution of permafrost can also affect local and regional groundwater flow [*Woo* et al., 2008; *Cheng and Jin*, 2013; *Kane et al*., 2013], but groundwater flow in cold regions has historically received little attention in the hydrological literature [*Woo et al*., 2008]. Recently, numerical groundwater flow models that consider freezing and thawing processes have been developed and applied to investigate the complex interactions between climate change, permafrost, and hydrogeology [e.g., *Bense et al*., 2009; *Frampton et al*., 2013; *McKenzie and Voss*, 2013; *Scheidegger and Bense*, 2014].

Several studies have reported observed multidecadal increases in baseflow in permafrost basins and have attributed these changes to enhanced suprapermafrost groundwater flow systems caused by recent permafrost thaw or less intense seasonal ground freezing [e.g., *Walvoord and Striegl*, 2007; *St. Jacques and Sauchyn*, 2009; *Sjöberg et al*., 2013]. This hypothesis does not account for the reduction in saturated hydraulic conductivity and related groundwater flow as the thaw depth and water table depth increase in organic soils [*Quinton et al*., 2008]. Permafrost thaw can also increase baseflow via enhanced deep groundwater circulation through intensified recharge and openings of taliks [*Walvoord et al*., 2012].

Also, observed increases in total streamflow in northern catchments have been attributed to increased surface hydrologic connectivity due to landscape changes caused by permafrost thaw [*Connon et al*., 2014]. For example, *Quinton et al*. [2011] demonstrated that the thawing of discontinuous permafrost in the Northwest Territories, Canada is causing a reduction in the area of forested peat plateaus (that impede the routing of water through the landscape due to underlying permafrost) and a concomitant expansion of unforested wetlands. The increasing fragmentation of forested peat plateaus results in a net loss of boreal forests [*Baltzer et al*., 2014], and affects the degree of surface hydrological connectivity of the intervening wetlands, and thus their role in runoff and storage processes [*Connon et al*., 2014]. The increase in surface hydrologic connectivity following permafrost thaw may be most important for discontinuous or sporadic permafrost regions experiencing rapid landscape changes [*Connon et al*., 2014]. Discontinuous permafrost is particularly vulnerable to climate warming as it is typically warmer and thinner than continuous permafrost [*McClymont et al*., 2013; *Sjöberg et al*., 2015]. However, most studies of observed permafrost thaw have focused on changes to the active layer thickness [e.g., *Kane et al*., 1991; *Nelson et al*., 1997; *Pang et al*., 2012] rather than changes to the lateral extent of discontinuous permafrost.

Previous studies of permafrost thaw have primarily been conducted using semiempirical, analytical, or numerical models of subsurface heat transfer that consider only vertical conductive heat transfer and the latent heat released or absorbed during freeze-thaw [e.g., *Riseborough et al*., 2008; *Zhang et al*., 2008a]. Emerging numerical models of coupled water flow and energy transport with freeze-thaw have facilitated investigations of multidimensional permafrost thaw and groundwater flow, but such studies have typically been restricted to two-dimensional simulations of idealized subsurface environments [e.g., *Ge et al*., 2011; *Bense et al*., 2012; *Frampton et al*., 2013]. *Noetzli et al*. [2007] conducted the first three-dimensional simulations of permafrost thaw due to climate change. Their boundary conditions represented alpine topography, which differs significantly from the topography of lowland discontinuous permafrost. Furthermore, their simulations, which neglected heat advection, were based on idealized scenarios rather than conditions from a specific field site. In general, there have been few modeling studies of multidecadal permafrost thaw that accommodate the influence of nonvertical heat transfer, and essentially none of these studies have been based on long term field observations.

The primary objective of the present study is to reproduce observed multidecadal (1970–2012) thaw and landscape transition of a peat plateau-wetland complex in the Northwest Territories, Canada using a process-oriented approach involving a surface energy model linked to a three-dimensional groundwater flow and heat transport model. The interdependency between landscape transition and permafrost thaw will be considered in detail. The secondary objective is to investigate the roles of lateral conduction, heat advection via groundwater flow, and heat transfer from open channel flow in accelerating permafrost thaw and landscape transition. In addition to investigating if permafrost thaw is influenced by the slow groundwater flow in the peatland, the simulations will also consider the influence of the permafrost on the local groundwater flow system. These simulations will help elucidate the fundamental drivers of permafrost thaw and associated landscape and hydrologic changes in discontinuous permafrost regions.

2. Site Description

This study addresses the thaw development of a single peat plateau-wetland complex ($<$0.1 km^2) within the Scotty Creek watershed, which is located south of the McKenzie River in the wetland-dominated discontinuous permafrost zone of the Northwest Territories, Canada (Figure 1a). This region has been experiencing pronounced climate warming [*Johannessen et al*., 2004] and permafrost thaw. The nearest long-term climate station is located 50 km north in Fort Simpson where the mean annual (1981–2010) air temperature and precipitation are, respectively, -2.5°C and 490 mm, with 46% falling as snow [*Environment Canada*, 2013].

The stratigraphy of the study site is characterized by an approximately 3 m thick organic layer overlying silty clay [*Quinton et al*., 2008]. The watershed landscape is a complex mosaic of peat plateaus, channel fens, and ombrotrophic flat bogs [*Quinton et al*., 2011]. The peat plateaus' ground surfaces rise 1–2 m above the surrounding wetlands and have a sparse canopy of black spruce trees and shrubs (Figure 1d). As is typical in discontinuous permafrost regions dominated by peatlands, the presence of the shading forest canopy and the thermal offset induced by the insulating peat [*Smith and Riseborough*, 2002] has preserved permafrost

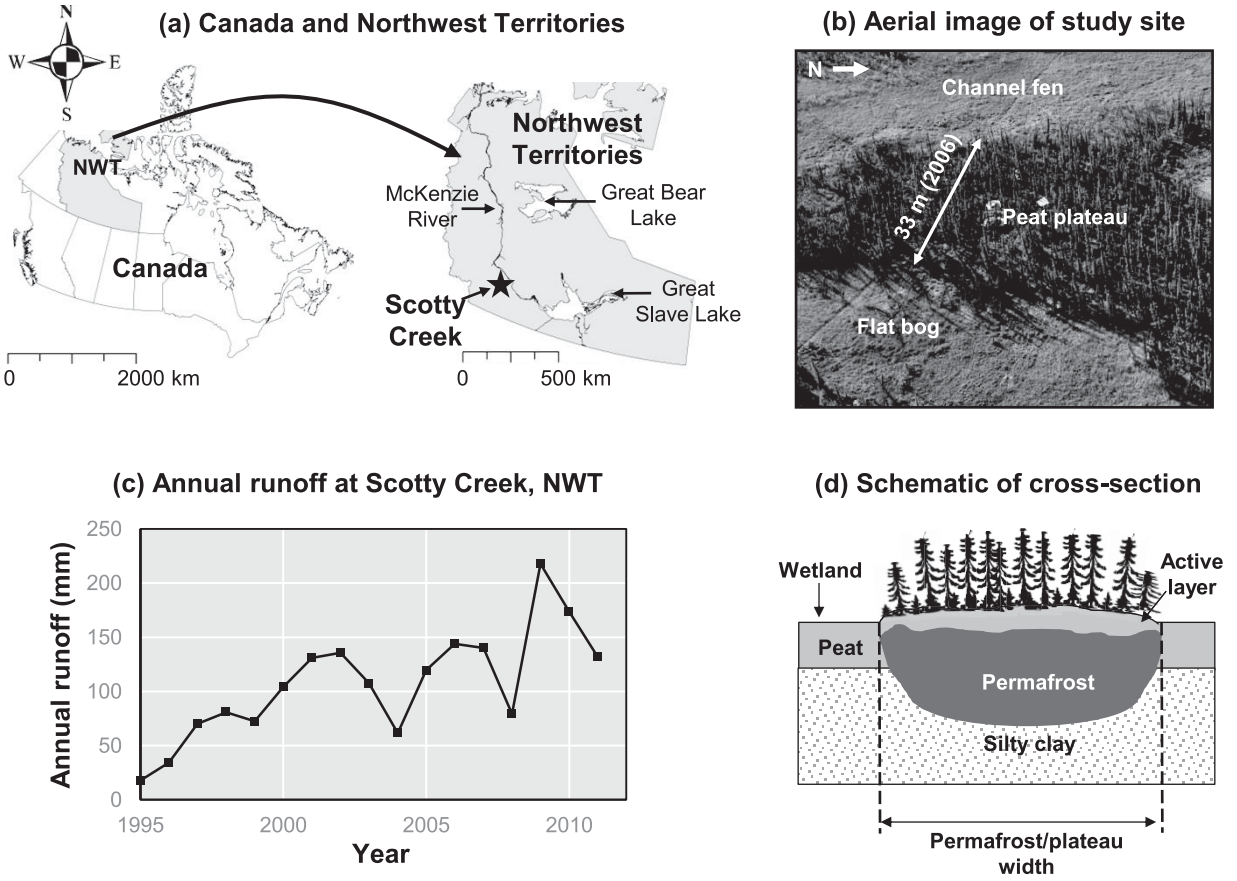

Figure 1. (a) Maps of Canada and the Northwest Territories, (b) September 2006 aerial image of the wetland-plateau complex in the Scotty Creek catchment considered in this study (lat. 61°18′48″ N, long. 121°18′24″ W), (c) annual runoff at Scotty Creek (data from the Water Survey of Canada), and (d) schematic of the cross section of the plateau-wetland complex considered in this study.

underlying the peat plateaus in the Scotty Creek watershed. In contrast, the wetlands surrounding the plateaus are permafrost free.

The three land cover types provide distinct hydrological functions in this region. The channel fens collect and convey water to the basin outlet [*Quinton et al*., 2003]. Bogs have varying degrees of hydrological connection with the basin drainage network. Since the elevation of the permafrost table beneath plateaus is higher than the elevation of the adjacent wetland surfaces, water in bogs that are completely surrounded by plateaus can only be lost via evaporation or groundwater recharge [*Wright et al*., 2008]. Other bogs are seasonally connected to the drainage network in accordance with the "fill and spill" mechanism [*Spence and Woo*, 2003]. Because they have similar surface energy balances, the bogs and fens are grouped together as "wetlands" in this modeling study. An aerial image of the particular plateau-wetland complex considered in this study (lat. 61°18′48″ N, long. −121°18′24″ W) is presented in Figure 1b, and a schematic of the cross section through this complex is shown in Figure 1d.

Over the past few decades, the landscape in the Scotty Creek catchment has transitioned from a plateau-dominated to wetland-dominated basin. *Quinton et al*. [2011] used aerial imagery to demonstrate that in 1970, 55% of the land surface area was covered with peat plateaus. As the permafrost underlying the plateaus thaws, the plateaus shrink and the wetlands expand. Consequently, the plateau land surface area decreased to 43% by 2008 [*Quinton et al*., 2011]. Based on this distribution of permafrost, this region would be strictly characterized by some as containing "sporadic permafrost," but herein we employ the alternative approach [e.g. *Woo*, 2012] of only distinguishing between continuous and discontinuous permafrost. In recent years, the annual runoff (stream discharge divided by drainage area) in the Scotty Creek watershed has increased substantially (Figure 1c). *Connon et al*. [2014] demonstrated that this increased runoff was not

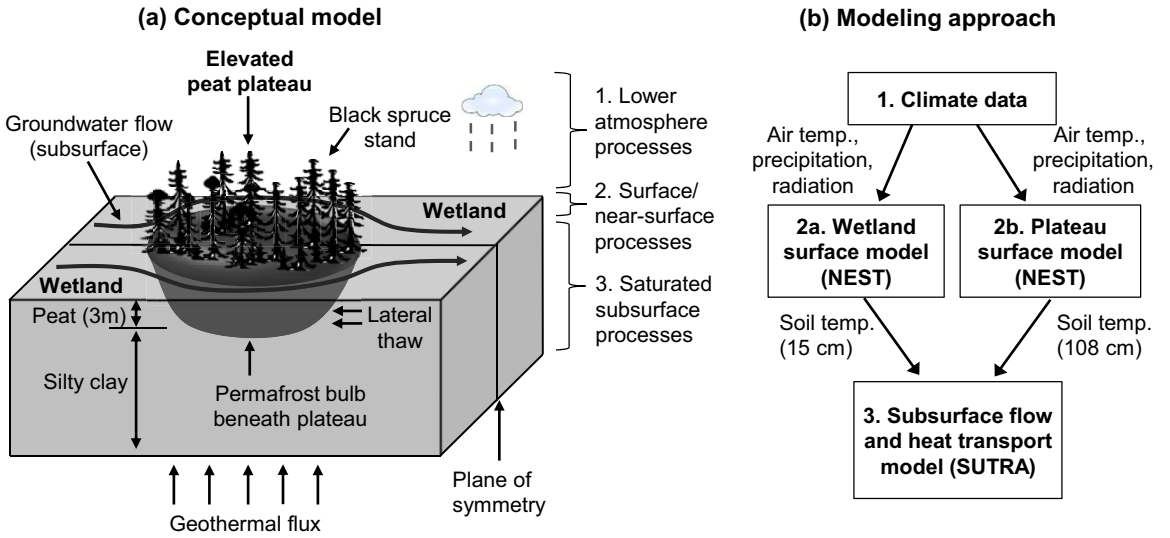

Figure 2. (a) Conceptual model depicting surface and subsurface thermal and hydrologic processes in the plateau-bog complex. (b) Flowchart depicting the flow of data in the sequential modeling approach. Note that the NEST simulations (step 2 in Figures 2a and 2b) actually extended down to a depth of 50 m, but the key output from the model was the near-surface soil temperature. The numbering in Figure 2a corresponds to the numbering in Figure 2b.

merely an artifact of increased precipitation and proposed that it was rather primarily due to the thaw-induced landscape transition and altered hydrologic connectivity.

The depth of seasonal thaw in the plateaus in the Scotty Creek catchment typically ranges between 0.5 and 1 m, and the seasonal freezing depth in the surrounding wetlands is normally about 0.3 m [*Hayashi et al*., 2007; *Wright et al*., 2009]. *McClymont et al*. [2013] used electrical resistivity tomography to demonstrate that the permafrost thickness beneath the particular peat plateau considered in the present study (Figures 1b and 1d) was estimated to be 9 ± 3 m in 2010. Like the other plateaus in the watershed, the width of this plateau has been decreasing rapidly since 1970 as discussed in more detail later.

3. Methods

3.1. Conceptual Model and Modeling Approach

Figure 2a presents the conceptual model of the hydrologic and thermal processes occurring in the peat plateau-wetland complex. This conceptual model is informed by several years of field investigations and site instrumentation [e.g., *Hayashi et al*., 2004, 2007; *Wright et al*., 2008]. An active groundwater flow system exists in the wetland in the upper layer of peat (3 m). The groundwater flows along the periphery of the permafrost body. The interrelationships between the local groundwater flow system and the permafrost body are investigated in this study. Beneath the peat layer, is a silty clay layer through which groundwater flow is negligible due to the low hydraulic conductivity ($K = 6 \times 10^{-10}$ m s^{-1}) [*Christensen*, 2014], and conduction is the dominant heat transfer mechanism.

Moisture and energy fluxes in the lower atmosphere control surface and near-surface temperatures, which in turn influence the thermal regime beneath the water table. These physical processes are simulated by adopting a sequential modeling approach as depicted in Figure 2b. Observed climate data are used to drive simulations of the surface energy balance and near-surface thermal processes in a soil-vegetation-atmosphere-transfer model. This model, NEST, described in section 3.3, accommodates surface processes, such as the thermal influence of the forest canopy and snowpack. The surface energy balance in the peat plateau differs from that in the surrounding wetlands due to the presence of the forest canopy as well as the underlying permafrost, which influences the ground heat flux. Simulations were performed separately for both land cover types (steps 2a and 2b, Figure 2b).

Heat transfer in the NEST surface model is represented only in the vertical dimension. Hence, near-surface soil temperatures from NEST are applied as the upper thermal boundary condition to a numerical model of three-dimensional groundwater flow and energy transport, SUTRA, described in section 3.4 (step 3,

Figure 2b). In this study, three dimensions are required for the SUTRA modeling in order to consider groundwater-permafrost interactions (Figure 2a). These models are run sequentially rather than coupled.

To avoid the need for simulating vadose zone processes in SUTRA, the top surface boundary was taken as the NEST-simulated soil temperature at the lowest seasonal position of the water table. Because the plateau surface is elevated about 90 cm with respect to the surrounding wetlands, the depth from the land surface to the water table during the dry season is greater beneath the plateau than beneath the wetland. In this study, the lowest seasonal position of the water table for the wetland was taken at a depth of 15 cm based on field observations. To achieve a horizontal plane for the top surface in SUTRA, the specified temperature for the plateau land cover type was taken as the NEST-simulated soil temperature at 1.08 m beneath the elevated plateau ground surface (Figure 2b). The approach of using a one-dimensional model that accommodates complex surface processes to form the upper boundary condition to a multidimensional subsurface heat transfer model is similar to that employed in previous studies [e.g., *Smith and Riseborough*, 2010; *McClymont et al*., 2013; *Kurylyk et al*., 2014b].

3.2. Measured Climate and Soil Temperature Data

The air temperatures from 1889 to 2004 used to drive the surface energy balance model were obtained from the *Environment Canada* [2015] meteorological station at Fort Simpson, Northwest Territories. Air temperatures for the period 2005–2012 were recorded at a meteorological station installed in the study site. Due to a 100 m elevation difference, air temperature recorded at the Fort Simpson station was on average 0.4°C colder than air temperature at our study site for 2005–2012. To investigate the influence of this temperature difference, simulations were performed using the same modeling approach described later but with a constant correction factor of -0.4°C applied for the 1889–2004 air temperatures. The results (not shown) indicated that this offset had little influence on the simulated thaw progression by 2012. Precipitation data were taken from the Fort Simpson station until 2008 [*Environment Canada*, 2015] and from the study site meteorological station after 2008 [*Christensen*, 2014].

In addition to air temperature and precipitation data, the surface energy balance model also requires daily values for vapor pressure, incoming shortwave radiation, wind speed, and cloud cover [*Zhang et al*., 2003]. The daily average vapor pressure was estimated in accordance with the air temperature-based method proposed by *Running et al*. [1987]. Incoming shortwave radiation was estimated from the site latitude, day of year, and the daily range in air temperature via the *Bristow and Campbell* [1984] method. The daily average cloud cover is only used in the surface energy balance model to estimate the net longwave radiation [*Zhang et al*., 2003]. In this study, cloud cover was not measured directly but was rather calculated from measured longwave radiation via the relationship between cloud cover and longwave radiation used in the surface energy model [*Zhang et al*., 2003]. Wind speed was measured at the meteorological station located in a flat bog at the study site from 2005 to 2012, and daily average values were computed. Prior to 2005, the daily cloud cover and wind speed were estimated from the average measured values obtained for each day of the year from 2005 to 2012, i.e., a representative year was used.

Soil temperatures in the study site were measured at multiple depths beneath a bog (wetland) and the peat plateau using thermistor probes (Campbell Scientific, 107) as described in *Hayashi et al*. [2007]. These instruments have an accuracy of $\pm$ 0.2°C. Measured soil temperature time series for 2005–2007 will be utilized to assess the performance of the surface energy balance model.

3.3. Surface/Near-Surface Model (NEST)

The Northern Ecosystem Soil Temperature (NEST) model [*Zhang et al*., 2003] was selected to simulate the surface and near-surface soil temperature (Step 2, Figure 2b). NEST has been applied at numerous permafrost sites in Canada [e.g., *Zhang et al*., 2008b, 2012]. In this study, NEST was driven with the previously described meteorological data from 1889 to 2012 for Fort Simpson and Scotty Creek.

The surface (ground surface or snow surface) temperature in NEST is obtained by balancing the energy fluxes based on the inputted climate data. The soil temperatures and, if applicable, snow temperatures are simulated by numerically solving the one-dimensional heat diffusion equation with an additional source/sink term to account for the latent heat of soil freeze-thaw. The bottom boundary condition in NEST is the geothermal heat flux, which was assigned a value of 0.08 W m^{-2} [*Blackwell and Richards*, 2004]. This was located at a depth of 50 m to limit the interactions of climate change and the geothermal flux. Initial conditions

(i.e., pre-1889) in NEST were generated with a 1250 year simulation to allow for the slow formation of the permafrost body from initially permafrost-free conditions using the NEST modifications for initial conditions described by *Christensen* [2014]. Air temperature data for this "spin-up" run from 1648 to1888 were obtained from climate data reconstructed from dendroclimatic data [*Szeicz and MacDonald*, 1995]. Air temperature data prior to 1648 were assumed to be static for 1000 years as pre-1648 climate conditions are highly uncertain for this region. Annual precipitation was generated for the spin-up simulation by randomly selecting one of the annual precipitation time series from 30 years (1964–1993) of measurements at the Fort Simpson station. Further details concerning how the NEST initial conditions were generated are provided by *Christensen* [2014].

3.4. Saturated Subsurface Model (SUTRA)

3.4.1. SUTRA Description

The multidimensional model selected for this study, SUTRA, is a finite element model of groundwater flow and heat transport [*Voss and Provost*, 2010] that has been recently enhanced to allow for pore water freezing and melting [*McKenzie et al*., 2007a]. The version of SUTRA that includes freeze-thaw has been applied to study subsurface temperature dynamics and groundwater flow in permafrost regions [*Ge et al*., 2011; *McKenzie and Voss*, 2013; *Wellman et al*., 2013; *Briggs et al*., 2014] and watersheds that experience seasonal freeze-thaw [*Kurylyk et al*., 2014b]. SUTRA is able to simulate freeze-thaw with variably saturated conditions, but, for the present study, only saturated conditions are considered as the unsaturated zone heat transfer is addressed in NEST.

3.4.2. SUTRA Governing Equations and Modifications

The governing energy transport equation in this version of SUTRA is:

$$C_{eff}\frac{\partial T}{\partial t}=-\varepsilon S_L\rho_L c_L \boldsymbol{v}\cdot\nabla T+\nabla\cdot(\lambda_{eff}\nabla T)+Q_p c_L(T^*-T)+\varepsilon S_L\rho_L\gamma_L+(1-\varepsilon)\,\rho_S\gamma_S \tag{1}$$

where C_{eff} is the effective volumetric heat capacity of the ice-water-soil matrix (J m^{-3}°C^{-1}), T is temperature (°C), t is time (s), ε is porosity, S_L is the liquid water saturation, ρ_L is the density of liquid water (kg m^{-3}), c_L is the specific heat of liquid water (4182 J kg^{-1}°C^{-1}), $\boldsymbol{v}$ is the groundwater velocity vector (m s^{-1}), λ_{eff} is the effective thermal conductivity of the ice-water-soil matrix (W m^{-1}°C^{-1}), Q_p is pore water inflow at a source or boundary (kg m^{-3} s^{-1}), T^* is the temperature of the inflowing water (°C), and γ_L and γ_S are the energy sources in the water and solid grains, respectively (J kg^{-1} s^{-1}). In this study, the last three terms in equation (1) are only relevant at the domain boundaries. Equation (1) was solved in three spatial dimensions. Note that the energy transfer equation in SUTRA is fully coupled to the groundwater flow equation. The temperature distribution influences the hydraulic conductivity field via the formation and melt of pore ice and changes to the fluid density and viscosity (although, as described below, density was held constant for the simulations in the present study), while the groundwater flux generates the advective heat flux as indicated by the first term on the right hand side of equation (1).

The effective heat capacity is equal to the weighted arithmetic average of the heat capacities of the matrix constituents plus latent heat effects during pore water phase change:

$$C_{eff}=\varepsilon(S_L\rho_L c_L+S_I\rho_I c_I)+(1-\varepsilon)\rho_S c_S-\Delta H_f\varepsilon\,\rho_I\frac{\partial S_I}{\partial T} \tag{2}$$

where ΔH_f is the latent heat of fusion for water (J kg^{-1}), S_I is the ice saturation, ρ_I is the ice density (kg m^{-3}), and c_I and c_S are the specific heats of the pore ice and soil grains, respectively (J kg^{-1}°C^{-1}).

SUTRA was modified for this study from the *McKenzie et al*. [2007a] formulation so that the effective thermal conductivity is computed as the volumetrically weighted geometric mean of the thermal conductivities of the matrix constituents [*Lunardini*, 1981]:

$$\lambda_{eff}=\lambda_L^{\varepsilon S_L}\lambda_I^{\varepsilon S_I}\lambda_s^{1-\varepsilon} \tag{3}$$

where λ_L, λ_I, and λ_s are the thermal conductivities of liquid water, ice, and the soil grains, respectively (W m^{-1}°C^{-1}). Usually, the effective thermal conductivity function in SUTRA includes an additional term for thermal dispersion [*Voss and Provost*, 2010]. However, there is ongoing debate on (1) the mathematical relationship (i.e., linear or nonlinear) between thermal dispersion and groundwater velocity [*Green et al*., 1964; *Sauty et al*., 1982; *Hopmans et al*., 2002; *Metzger et al*., 2004; *Rau et al*., 2012], (2) the magnitude of thermal dispersivity compared to solute dispersivity [*Smith and Chapman*, 1983; *de Marsily*, 1986, p. 279; *Constantz*

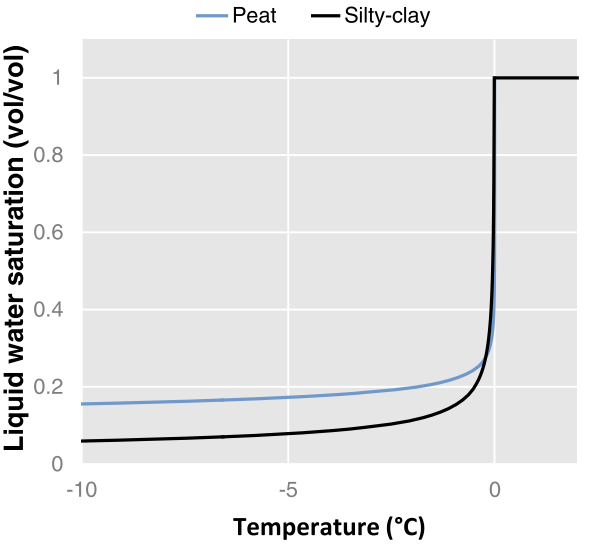

Figure 3. Soil freezing curves used in SUTRA.

et al., 2003; *Anderson*, 2005], and (3) the appropriateness of considering thermal dispersion as a transport process due to the underlying differences in solute and heat transport processes [*Bear*, 1972; *Ingebritsen and Sanford*, 1998]. Thus, thermal dispersion was assumed to be negligible in the present study (i.e., the thermal dispersivity value in SUTRA was set to 0), which is often the recommended approach [e.g., *Ingebritsen and Sanford*, 1998, p. 81].

Table A1 lists the constituent thermal properties used in SUTRA. These values yielded bulk unfrozen soil thermal conductivities of 0.50 W $m^{-1}°C^{-1}$ for the saturated peat and 1.08 W $m^{-1}°C^{-1}$ for the saturated silty clay, which concur with measured values of peat at the field site [*Hayashi et al*., 2007] and literature values of silty clay [*Jury and Horton*, 2004].

Adjustments to the SUTRA code were also made to allow for a power function soil freezing curve:

$$S_L = \alpha(-T)^{\beta} \tag{4}$$

where α and β are empirical fitting parameters to relate the remaining liquid water saturation to subfreezing soil temperatures [*Andersland and Ladanyi*, 1994]. The liquid saturation was constrained to be $\leq$1. If the temperature is greater than 0°C, then S_L is 1. Figure 3 presents the soil freezing curves that were used for the SUTRA simulations. The parameters for these curves were determined from field measurements at the study site [*Zhang et al*., 2008a] and are listed in Table A1.

SUTRA was further modified so that the land cover type (peat plateau or wetland) for each top surface node of the domain was automatically updated as it changed for each simulation year. This was accomplished with a subroutine that read through the temperature array for the rectilinear mesh at the end of each summer thawing period (mid-September) and assigned a land cover type of plateau or wetland depending on the presence or absence of permafrost (subfreezing temperature) in each underlying column of nodes.

For these simulations, the fluid density function in SUTRA was set to be constant (independent of temperature) for simplicity and to reduce the nonlinearity of the governing flow and energy transport equations. Thus the water flux was equal to the product of the hydraulic conductivity and the hydraulic gradient in accordance with Darcy's law applied for constant density fluids. In order to account for the hydraulic resistance of pore ice [*Kurylyk and Watanabe*, 2013], a simple relative hydraulic conductivity function was selected that decreases linearly with ice saturation [e.g., *McKenzie et al*., 2007a] until achieving a minimum relative hydraulic conductivity (1×10^{-8}) at residual liquid saturation (0.1). The actual hydraulic conductivity was calculated as the product of the relative hydraulic conductivity and the unfrozen, saturated hydraulic conductivity. Hydraulic parameters are provided in Table A1.

3.4.3. SUTRA Domain Details and Boundary Conditions

Figure 4 presents the modeling domain employed in SUTRA. The plan view dimensions of each element were 1 m by 1m. The vertical element dimension was smaller at the top of the mesh (0.1 m) and increased toward the bottom (3.5 m) to accommodate the daily and seasonal temperature variations near the ground surface. Mesh refinement studies were conducted, and finer meshes did not produce significantly different results. SUTRA simulations were performed with a daily time step from 1970 to 2012 with leap days ignored (15,695 time steps). Simulations were performed for one half of the plateau-wetland complex due to the system symmetry (Figure 2a). More details concerning the finite element mesh, the numerical solver controls, and the time step size are provided in Table A1.

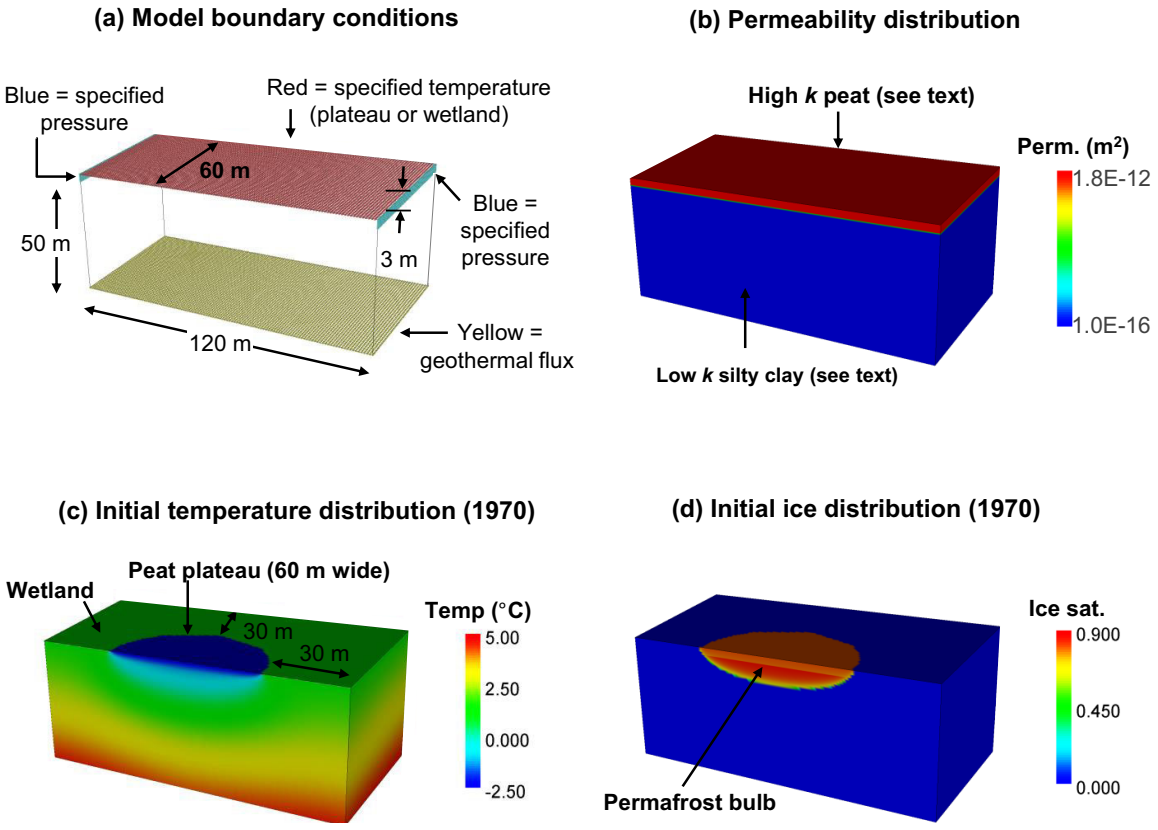

Figure 4. Conditions for SUTRA modeling domain: (a) boundary conditions (*Unless otherwise specified, all boundaries were no-flow and perfectly insulating boundaries; see text for explanation. The specified pressure boundary conditions also required that the temperature of the inflowing water be specified), (b) permeability distribution, (c) initial temperature distribution, and (d) initial ice saturation distribution. The permeability shown in Figure 4b only corresponds to one simulation as different permeability distributions were considered (Table 1).

The top surface of the SUTRA domain was a specified temperature boundary condition determined by the output from the NEST simulations at the seasonally lowest point of the water table (Figure 4a). The specified temperatures along the upper surface varied laterally with two potential values depending on whether a surface node was identified as underlying a peat plateau or a wetland (section 3.4.2). A geothermal heat flux of 0.08 W m^{-2} was assigned across the bottom of the model domain at a depth of 50 m [*Blackwell and Richards*, 2004], consistent with the bottom boundary condition for NEST. Unless otherwise specified, all other thermal boundary conditions were perfectly insulating with the locations of the insulating boundaries based on the distance between nearby peat plateaus. For example, the distance from the perimeter of the plateau in 1970 to the insulating boundary conditions (vertical surface, Figure 4c) was chosen to be 30 m based on the total 60 m distance to the next peat plateau in 1970 [*Quinton et al.*, 2011]. For most of the simulations, the temperature of the incoming water (see hydraulic boundary conditions discussion below) at the left hand boundary (Figure 4a) was set to the daily wetland soil temperature at 15 cm depth simulated in NEST. To examine the influence of the specified inflow temperature, simulations were also performed with the temperature of the inflowing water set to the simulated soil temperature at the halfway depth of the peat layer (1.5 m) and at the halfway depth of the upper 0.5 m high hydraulic conductivity layer (see below).

Specified pressure boundary conditions were assigned along the left and right vertical faces of the domain for the peat layer in the upper 3 m (Figures 4a). These boundary conditions imposed a horizontal hydraulic gradient of 0.003, which was selected based on the average land surface slope in the Scotty Creek watershed. The pressure boundary conditions were only assigned along the top 3 m for most runs because this is the zone of relatively high permeability and groundwater flow rates (Figure 4b) and because the inflowing water temperature must be specified in SUTRA. The temperature of the inflowing water in the shallow peat layer could be estimated from the NEST output (as described above), but the temperatures deeper in the

Table 1. SUTRA Scenarios Considering Different Peat Hydraulic Conductivities

Scenario	K in Upper 50 cm of Peat (m s^{-1})	K in Lower Peat Zone (m s^{-1})
1	1×10^{-5}	1×10^{-5}
2	1×10^{-4}	1×10^{-4}
3	1×10^{-4}	1×10^{-5}
4	1×10^{-3}	1×10^{-5}

domain (i.e., up to 50 m) could generally be influenced by lateral heat transfer and may not be reasonably represented by the NEST output. To test the importance of the vertical extent of this boundary condition, a simulation was also conducted with the specified pressure boundaries imposed along the entire vertical thickness of the SUTRA domain (50 m) and with the temperature of the inflowing water specified in accordance with the general geothermal gradient. The simulated thaw rates for this run were unchanged in comparison to the runs conducted with pressure boundary conditions only imposed along the upper peat layer (top 3 m, Figure 4a). Simulations were also performed with no hydraulic gradient to compare thaw rates with and without heat advection considered. All other domain boundaries were no-flow hydraulic boundaries.

The saturated hydraulic conductivity of the peat layer in the study site is known to decrease with depth [*Quinton et al*., 2008], and the hydraulic conductivity of the silty clay is several orders of magnitude lower than that of the peat. Since the hydraulic conductivity (K, m s^{-1}) varies with temperature-dependent viscosity [*Freeze and Cherry*, 1979, p.27], SUTRA uses the intrinsic permeability (k, m^2) to specify the material hydraulic property. As shown in the results section, the overall average temperature of the nonpermafrost part of the model domain was approximately 4°C. Therefore, a viscosity value of 1.57×10^{-3} kg m^{-1} s^{-1} at 4°C [*Huber et al*., 2009] will be used in the following to indicate the correspondence between k and K. In this study, a uniform permeability of 1.0×10^{-16} m^2 ($K = 6 \times 10^{-10}$ m s^{-1}) was assigned for the silty clay based on the slug tests results of *Christensen* [2014]. Four separate permeability distributions were considered for the upper 3 m peat layer (Table 1). For the first scenario, a uniform permeability of 1.8×10^{-12} m^2 ($K = 1 \times 10^{-5}$ m s^{-1}) was assigned for the entire peat layer based on slug tests performed below 50 cm in the peat layer [*Christensen*, 2014]. Second, the uniform permeability for the peat layer was increased by an order of magnitude ($K = 1 \times 10^{-4}$ m s^{-1}). The third and fourth scenarios were the same as the first scenario except that the permeability in the upper 50 cm of soil was increased to 1.8×10^{-11} m^2 ($K = 1 \times 10^{-4}$ m s^{-1}) for the third scenario and 1.8×10^{-10} m^2 ($K = 1 \times 10^{-3}$ m s^{-1}) for the fourth scenario to account for the enhanced hydraulic conductivity at shallow depths in the study site [*Quinton et al*., 2008].

3.4.4. SUTRA Initial Conditions

It is difficult to accurately determine the dimensions of the peat plateau considered in this study (Figure 1b) from aerial images before 1970. Thus, the SUTRA simulations were begun in 1970. The depth of the permafrost in 1970 is unknown, and hence the initial temperature conditions and permafrost depth were generated by running a steady state simulation in SUTRA. This steady state run was forced using different temperatures applied along the top surface for the two land cover types (wetland and plateau). The initial aerial dimensions of the plateau were assumed to be approximately circular with a diameter of 60 m in accordance with the aerial image from 1970 [*Quinton et al*., 2011]. A constant temperature less than 0°C was applied for the plateau land cover type to generate the initial body of permafrost, while a constant temperature greater than 0°C was applied for the wetland to generate permafrost-free conditions.

Multiple steady state simulations were initially performed to generate different initial (1970) permafrost depths by varying the specified temperatures at the top boundary by intervals of 0.25°C. These different initial conditions were then perturbed in transient simulations using the near-surface soil temperature in NEST to assess whether the 1970–2012 simulated rate of permafrost thaw concurred with the observations. Results presented hereafter were obtained with initial conditions generated by running a steady state simulation with a specified temperature of −2.5°C for the top surface for the plateau land cover type and 1.3°C for the wetland. This steady state run produced a permafrost bulb with a depth of 12.5 m. The thickness of the permafrost body for the steady-state runs was somewhat sensitive to the choice of the specified surface temperature for the plateau. For example, if the specified temperature overlying the permafrost for the steady state run was reduced to −3°C, the depth to the base of permafrost increased to 13.5 m. The initial temperature and ice saturation distributions for this steady state run are presented in Figures 4c and 4d, respectively. The initial pressure distribution was hydrostatic across the domain with a pressure of 0 Pa at the top surface.

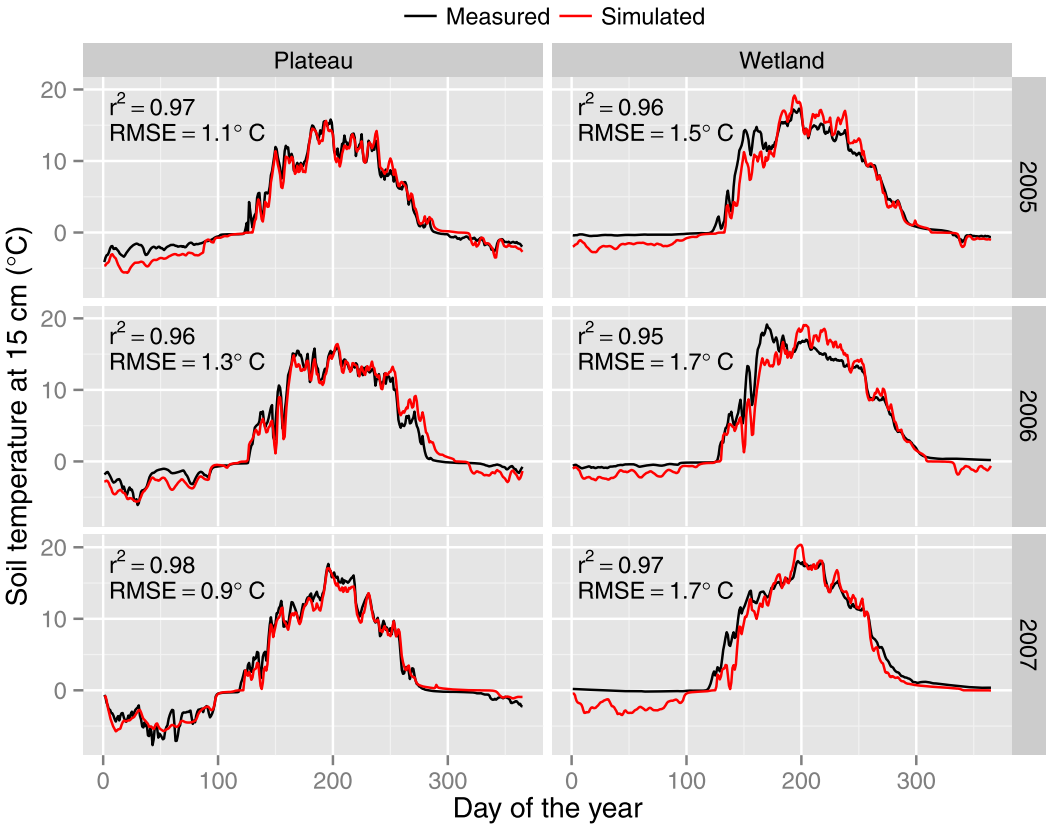

Figure 5. Measured (black) and simulated (red) soil temperature for the plateau (left) and wetland (right) for 2005, 2006, and 2007. The soil temperatures beneath the plateau were directly measured at 15 cm. The measured soil temperatures for the wetland were obtained by linearly interpolating between the soil temperature recorded at depths of 10 and 30 cm.

The appropriateness of these initial temperature and ice conditions can be assessed by comparing the simulated reduction in the permafrost width from 1970 to 2012 to the observed shrinking of the plateau during this period and by comparing the simulated permafrost thickness in 2010 to that estimated by *McClymont et al*. [2013] from a geophysical survey.

3.5. Analysis of Thermal Effects of Surface Water Flow

During the summer months, open channel flow occurs within a narrow channel that borders the plateau. Simple 2-D SUTRA simulations with smaller elements were conducted to estimate the thermal influence of this ephemeral, but rapid, surface water flow. These were conducted by assigning a very high hydraulic conductivity zone in the vicinity of the channel. Further information is provided in supporting information.

4. Results

4.1. NEST Results

4.1.1. Comparison of NEST Results to Field Data

To assess the performance of the NEST model, simulated soil temperatures for 2005–2007 were compared to measured soil temperatures in the study site beneath the wetland and plateau (Figure 5). Measured and simulated soil temperatures for both land cover types are shown for a depth of 15 cm, which is the depth of the SUTRA surface boundary condition for the wetland (step 2b, Figure 2b). As indicated by the root-mean-square-error (*RMSE*) and coefficient of determination (R^2) presented in Figure 5, the NEST model performed better for the plateau than for the wetland. The average R^2 and *RMSE* values were 0.97 and 1.1°C for the plateau, and 0.96 and 1.7°C for the wetland.

4.1.2. Long-Term Climate Data and NEST Results (1900–2012)

The long-term air temperature data shown in Figure 6a indicate that significant climate warming occurred in the region from 1900 to 2012 at a rate of approximately 0.02°C yr^{-1}. The warming rate during this period

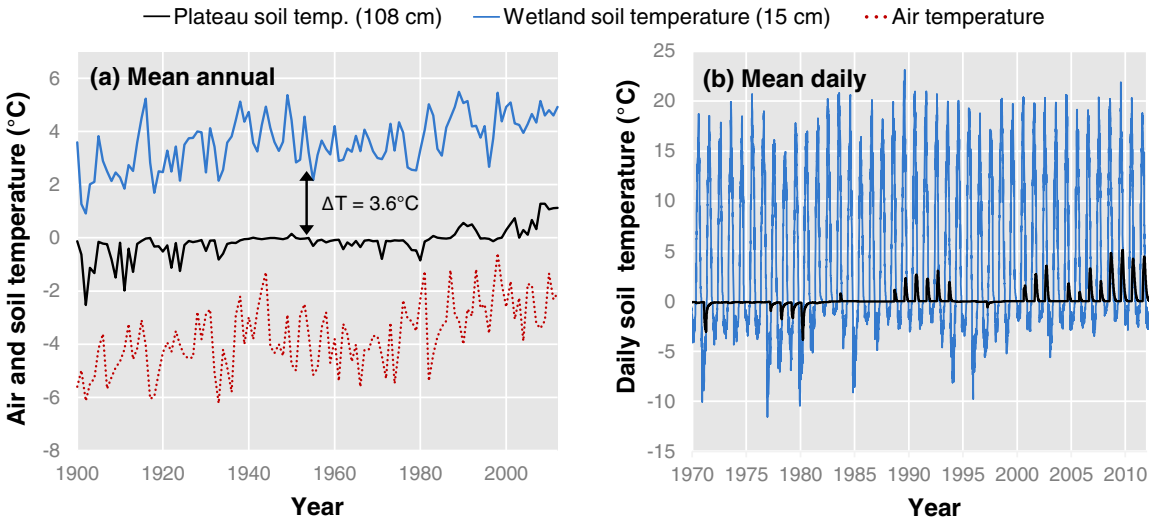

Figure 6. (a) Measured mean annual air temperature and NEST-simulated mean annual soil temperature for the plateau (108 cm) and the wetland (15 cm) for 1900–2012. (b). Daily simulated 1970–2012 soil temperature for the wetland (15 cm) and the plateau (108 cm).

was not constant, with a relatively stable period during 1945–1978. The other series presented in Figure 6a depict the simulated soil temperatures when the observed air temperature data were used to drive NEST simulations for the peat plateau and wetland. These soil temperature data are presented at the seasonally lowest point of the water table for the wetland and peat plateau (0.15 and 1.08 m, respectively). On average, there is a simulated temperature difference of approximately 3.6°C between the mean annual soil temperature beneath the wetland and the plateau due to the shading influence of the forest canopy and the cooling effect of the underlying permafrost. Figure 6b presents the daily simulated soil temperatures beneath the wetland and the peat plateau from 1970 to 2012. These series represent the daily specified top surface temperatures for the SUTRA simulations (Figure 4a). The NEST simulations also indicated that the combined thickness of the active layer and the perennially unfrozen zone above the permafrost table increased from 0.85 m in 1970 to 2.51 m in 2012.

4.2. SUTRA Results

4.2.1. SUTRA-Simulated Permafrost Thaw

The initial lateral extent of the peat plateau, and hence the underlying permafrost body, were obtained from aerial imagery from 1970 [*Quinton et al.*, 2011]. The plateau widths were measured in situ annually from 1999 to 2012. Figure 7a presents the observed shrinking of the plateau from 1970 (60 m wide) to 2012 (20.2 m wide). The SUTRA results in Figure 7a represent the simulations initiated with the steady state temperature distribution shown in Figure 4c and forced using the plateau and wetland soil temperature presented in Figure 6b. The simulations were performed with only heat conduction considered; the influence of heat advection will be discussed later. The simulated width of the permafrost body decreases from 60 m in 1970 to 22.9 m by 2012, which is similar to the observed reduction in plateau width during this period. Much of this lateral reduction in plateau width could be due to vertical thawing at the edges where the permafrost is thinner (Figure 4d), and this effect could potentially be captured in a distributed 1-D heat transfer model. To test the importance of lateral heat transfer, SUTRA simulations were also performed with an anisotropic thermal conductivity, i.e., the vertical conductivity was left unchanged (Table A1) but the horizontal (*x-y*) plane thermal conductivity was set to 0. Figure 7a indicates that importance of lateral conduction in these simulations increased over time as the size of the permafrost body decreased.

Figure 7b presents the simulated maximum depth to the base of the permafrost body, which decreased from 12.5 m in 1970 to 8.8 m in 2012. Only results with full 3-D heat transfer are presented as the results with no lateral conduction were similar. The step function appearance of this trend stems from the coarser mesh employed at this depth (Table A1). *McClymont et al.* [2013] used the results from an electrical resistivity survey to estimate the thickness of the permafrost body to be 9 ± 3m in 2010. The depth to the

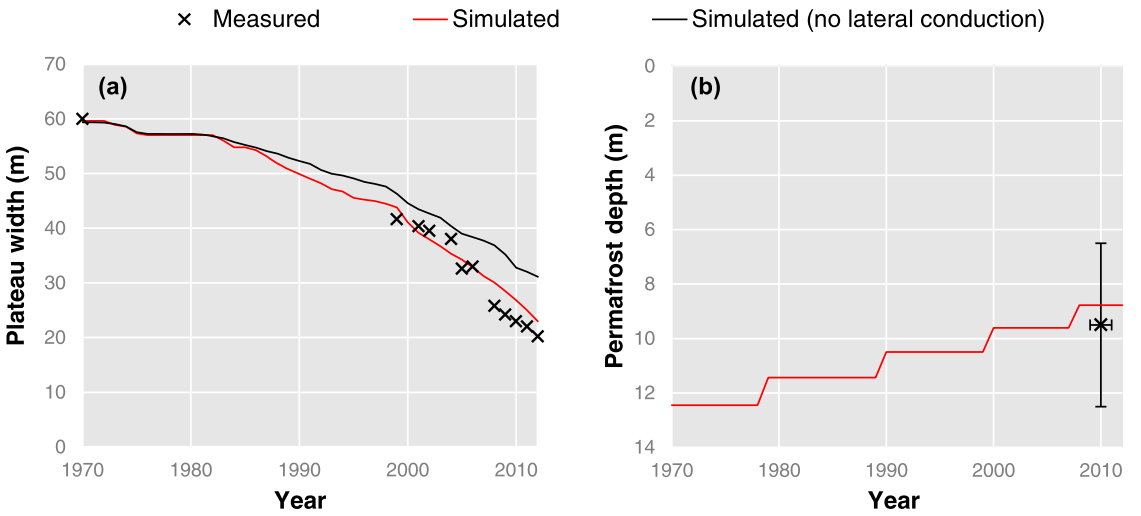

Figure 7. (a) SUTRA-simulated and measured plateau widths versus time from 1970 to 2012. (b) SUTRA-simulated depth to the permafrost base from 1970 to 2012. The permafrost depth (permafrost thickness plus active layer thickness) estimated by *McClymont et al.* [2013] in 2010 is also presented. The step-like nature of Figure 7b is due to the coarser vertical element dimension at this depth (~1 m). Error bars denote combination of uncertainty and spatial variability in measurement.

permafrost base can be obtained by adding the estimated permafrost thickness to the active layer thickness (Figure 7b).

4.2.2. Groundwater Flow Results and the Influence on Thaw Rate

SUTRA simulations that included groundwater flow and associated heat advection were also conducted. These differed based on the peat layer hydraulic conductivity distribution and the temperature of the inflowing water as described in section 3.4.3 and Table 1. Each of these simulations was started with the same 1970 initial temperature and ice distributions as the simulation that considered only heat conduction (Figures 4c and 4d). All of the SUTRA simulations that included groundwater flow resulted in thaw rates and changes in the dimensions of the permafrost body that were essentially identical to the results produced with only heat conduction considered (Figure 7). Thus the heat advection due to groundwater flow does not significantly contribute to multidecadal thaw at this field site. This is likely due to the low hydraulic conductivity of silty clay and hence the low groundwater flow rates and heat advection.

Figure 8a presents the total simulated groundwater flow entering the SUTRA domain averaged for each day of the year from 1970 to 2012 for the four different hydraulic conductivity scenarios (Table 1). Because the water density is constant and the wetland hydraulic gradient is fixed at 0.003, the groundwater flow rate is only dependent on the hydraulic conductivity. Groundwater flow decreases during the winter months as near-surface pore ice forms and hydraulic conductivity decreases. As expected, simulations performed with higher unfrozen, saturated hydraulic conductivities resulted in higher groundwater flow rates throughout the year (Scenarios 2 and 4, Figure 8a). In the absence of pore ice, total groundwater flow should be equivalent to the product of the saturated, unfrozen peat hydraulic conductivity, hydraulic gradient, and cross-sectional area of the peat layer (i.e., 3 m $\times$ 60 m, Figure 4a). Figure 8a (dashed lines) presents the theoretical maximum groundwater flow rates for each simulation scenario if there were no pore ice in the flow domain. Even when the wetland is unfrozen in the summer, the groundwater flow through the wetland does not attain these theoretical maxima due to the plateau-scale hydraulic impedance as the groundwater encounters the permafrost "dam" (Figure 2a).

The total annual groundwater flow through the SUTRA domain increased throughout the simulation due to the gradual degradation of the permafrost body and the consequent decrease in the plateau-scale hydraulic impedance (Figure 8b). For example, the total annual groundwater flow through the SUTRA domain for scenario 2 (Table 1) was 1100 m^3 in 1970 and increased to 1410 m^3 by 2012 (Figure 8b).

4.2.3. SUTRA Energy Balance

As shown in Figure 4a, energy enters the SUTRA domain via the geothermal heat flux at the base of the domain, the specified temperature at the top surface, and the lateral inflow of groundwater. Figure 9 presents the energy flows (fluxes times area) for each of these noninsulating thermal boundary conditions

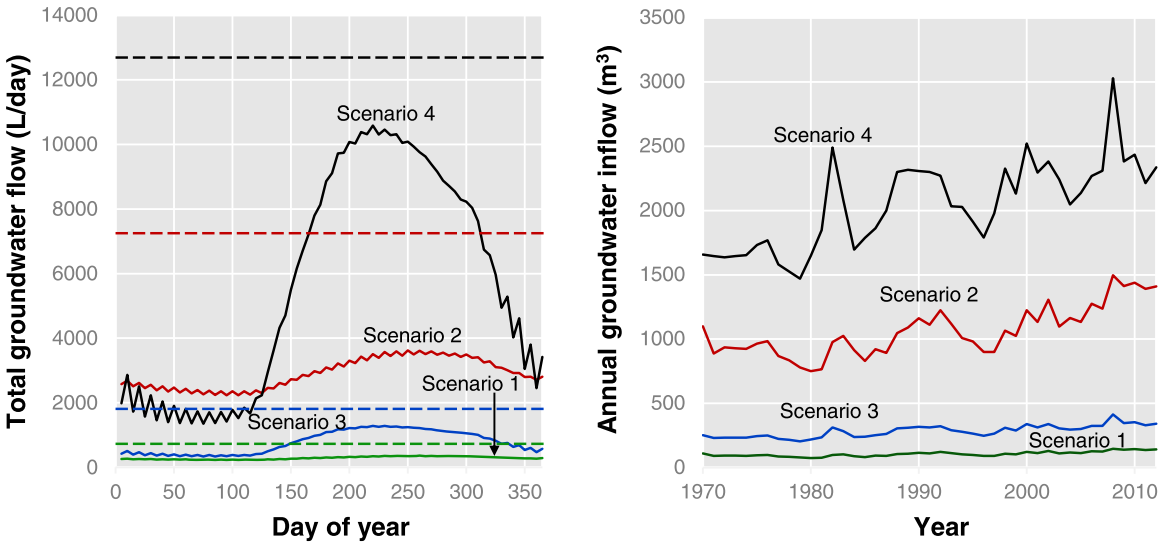

Figure 8. (a) Simulated total groundwater flow rates (recorded at the inflow boundary) averaged for each day of the year from 1970 to 2012 for the scenarios with groundwater considered (see Table 1). Results are presented for the simulations with the inflow temperature set to the NEST-simulated wetland temperature at 15 cm depth. Dashed lines indicate theoretical maximum (ice free) groundwater inflow as described in the text. (b) Simulated total annual groundwater inflow versus year for each of the scenarios in Figure 8a.

averaged for each day of the year from 1970 to 2012. In SUTRA, the advective heat flow at a boundary is calculated by summing the product of the groundwater discharge, volumetric heat capacity of water, and groundwater temperature (°C) for all nodes at the inflow/outflow boundary. If the temperature is above 0°C, groundwater entering the model produces a positive energy flux, and groundwater leaving the model produces a negative energy flux (Figure 9a) i.e., the thermal datum is 0°C [*Kurylyk et al.*, 2015]. Figure 9a indicates that the net heat advection due to the inflow and outflow is positive in the summer. This is because groundwater cools as it flows around the permafrost body during the summer months (Figure 2a), and thus groundwater entering the model is generally at a higher temperature than groundwater leaving the model. The results are only presented for the scenario with the highest groundwater flow (i.e., Scenario 4, Figure 8) to illustrate the maximum relative influence of groundwater flow. During the summer months, the net

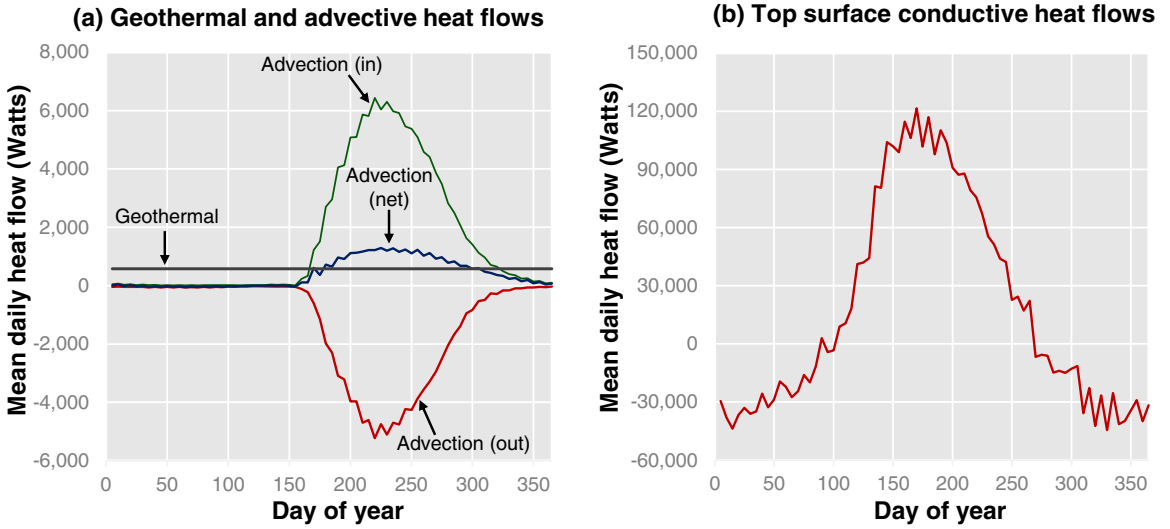

Figure 9. (a) The heat flows associated with the inflow/outflow of groundwater and the bottom geothermal boundary condition and (b) The conductive heat flux entering the model domain through the specified temperature nodes at the upper surface. Both Figures 9a and 9b are averaged for each day of the year from 1970 to 2012. Results are presented for Scenario 4 (Table 1) when the inflowing water was specified as the NEST-simulated wetland temperature halfway through the upper 0.5 m layer.

advective heat flow is typically higher than the temporally constant geothermal heat flow, but the geothermal heat flow is greater than the net advective heat flow during the colder months (Figure 9a).

The simple two-dimensional SUTRA analysis presented in supporting information suggests that the mean annual advection due to the ephemeral surface water flow in the channel bordering the plateau is less than the mean annual advection due to local groundwater flow.

Figure 9b presents the mean daily conductive heat flows entering the model via the top specified temperature boundary condition (Figure 4a). A comparison of Figures 9a and 9b (note the difference in the vertical axes scales) indicates that heat advection is only a minor energy input to the SUTRA domain even for the scenario with the highest groundwater flow rates. This analysis illustrates why the thaw rates obtained from simulations with only heat conduction considered were similar to results obtained from simulations with groundwater advection included. The conductive heat flux is positive during the summer when the warm near-surface soil temperature signals are diffused into the SUTRA domain. Conversely, in the winter, the top boundary condition is cooling the SUTRA domain, and the incoming conductive flux is negative. On average throughout the year, a positive energy flow enters the specified temperature boundary condition as the permafrost is in disequilibrium with the climate.

5. Discussion

5.1. Discussion of NEST Results

The NEST model generally produced the observed seasonal trends in soil temperatures beneath the wetland and plateau (Figure 5). However, the measured soil temperatures beneath the wetland exhibited fewer fluctuations during the winter period than the simulated soil temperatures. This could potentially arise due to the actual soil moisture being higher than the simulated soil moisture during the winter months. Soils with higher moisture contents tend to remain closer to 0°C during the winter months due to the thermal inertia associated with latent heat of freeze-thaw [*Williams and Smith*, 1989]. It is possible that the upward flow of moisture driven by cryosuction may be an important process affecting winter heat transfer at this site [*Nagare et al*., 2012]. Alternatively, a slight underestimation of snow depth in NEST [*Christensen*, 2014] may have contributed to the high seasonal soil temperature variability.

The NEST simulations indicate that the near-surface thermal regime rapidly responds to warming air temperatures. For example, the simulated average linear increases in mean annual soil temperature at 15 cm in the wetland (0.035°C yr^{-1}) and 108 cm in the plateau (0.030°C yr^{-1}) from 1970 to 2012 are approximately the same as the air temperature warming rate during this period (Figure 6a). The wetland soil temperatures presented in Figure 6b exhibit more seasonal variability than the peat plateau soil temperatures due to the shallower depth and the absence of permafrost in the case of the wetland.

5.2. Discussion of SUTRA Results

5.2.1. Simulated Thaw Development (Past and Future)

The similarity between the simulated and measured trends in the width of the peat plateau and underlying permafrost body from 1970 to 2012 (Figure 7a) supports the choice of the initial temperature and ice distributions for 1970 (Figures 4c and 4d). Furthermore, the 2010 permafrost depth simulated in SUTRA is close to that estimated from an electrical resistivity survey in 2010 (Figure 7b). The slight differences between the SUTRA simulation results and field data may arise in part because the peat plateau perimeter is not completely circular as it was represented in SUTRA (Figure 1b). In general, the congruence of the simulated and observed thaw development of the plateau-wetland complex suggest that the important heat transfer processes are adequately represented in the conceptual modeling framework and the corresponding SUTRA simulations.

Figure 7a indicates that the plateau width decreased by about 40 m (66%) from 1970 to 2012, whereas the simulated change in the maximum depth of the permafrost body was about an order of magnitude less (3.7 m) during this same period (Figure 7b). Figure 7a also indicates that simulations considering and ignoring lateral conduction produced essentially identical results up to 1985 and diverged after that point. These results are intuitive as the initial permafrost body was thinner and had lower initial ice content around the plateau edges (Figure 4d), and vertical heat transfer could rapidly thaw through this permafrost and produce a decrease in width. However, once only thicker permafrost remained, the importance of lateral heat

transfer increased. For example, the reduction in permafrost width from 2005 to 2012 was 43% higher for the simulation with lateral heat transfer considered (Figure 7a). The importance of lateral heat transfer has also been demonstrated for steep mountainous environments [*Noetzli et al*., 2007; *Noetzli and Gruber*, 2009]. However, in alpine environments, topography is one of the primary controls on lateral heat transfer, whereas at our study site, the complex landscape mosaic and patchy permafrost distribution induces lateral heat transfer.

Additional SUTRA simulations were conducted to investigate future thaw development and associated landscape transition of the peat plateau-wetland complex. The initial conditions for these simulations were taken as the temperature and pore ice distributions simulated at the end of 2012. The top surface boundary condition was generated with results from NEST simulations extending to 2050. One NEST simulation was driven by repeating the climate data from 2001 to 2012. Additional NEST simulations were run by assuming different linear air temperature warming rates of 0.01, 0.03, and 0.07°C yr^{-1} superimposed on the repeating climate data from 2001 to 2012 to represent the average warming rates projected for the study site [*Pacific Climate Impacts Consortium*, 2014] for representative concentration pathways 26, 45, and 85, respectively [*van Vuuren et al*., 2011]. In each of the 2012–2050 SUTRA simulations, the peat plateau completely disappears within 5 years. The remnant permafrost beneath the peat plateau is in such disequilibrium with the current climate, that the resilience of the permafrost is not influenced by the selection of the climate warming scenario. This remarkable thaw rate is indicative of a potential runaway effect once the permafrost warms and the pore ice content decreases in accordance with the soil freezing curve (equation (4)). A reduction in pore ice content causes a proportional decrease in the energy required to thaw a given volume of soil.

5.2.2. Interrelationship Between Groundwater Flow and Permafrost

The gradual degradation of the permafrost body resulted in enhanced groundwater flow through the peat plateau-wetland complex (Figure 8b). As elevated peat plateau "dams" shrink, formerly disconnected channel fens and flat bogs may become increasingly connected through activated groundwater flow systems. This increase in simulated groundwater discharge may explain in part the apparent increase in the landscape hydrologic connectivity and the increases to measured discharge in Scotty Creek (Figure 1c). Bogs that were formerly disconnected (or poorly connected) to the basin outlet may more efficiently transmit water through surface and subsurface flow paths opened up by thawing permafrost. The corresponding increase in basin contributing area can lead to enhanced streamflow.

Results from the SUTRA simulations indicate that groundwater flow does not contribute significantly to the thawing of the permafrost body considered in this study. The lack of influence of groundwater flow arises due to the dominance of heat conduction from the land surface (Figure 9). In general, the influence of groundwater flow on permafrost thaw depends on many factors, including "the proximity to surface water bodies, the timing and magnitude of precipitation, local and regional topography, and the existence and distribution of taliks" [*Kurylyk et al*., 2014a]. The results of the present study concur with the findings of *Bense et al*. [2012], who demonstrated that advection is not normally a significant permafrost thawing process except in certain hydrogeological scenarios. *McKenzie et al*. [2007b] also demonstrated via field data that heat advection via groundwater flow is typically not important in peatlands.

Groundwater flow is highest during the summer months when the active layer is fully thawed (Figure 8), thus the groundwater temperature during the hydraulically active period is warmer than the mean annual surface temperature. Consequently, the advective heat flux typically produces a positive net energy flow to the perimeter of the permafrost body (Figure 9a). It is reasonable then to suggest that groundwater flow may contribute to discontinuous permafrost thaw in catchments with a higher hydraulic gradient or more permeable soils. For example, *Sjöberg et al*. [2016] found that heat advection via groundwater flow sourced from nearby lakes can be an important heat transfer mechanism in a discontinuous permafrost site in northern Sweden.

The three-dimensional SUTRA simulations presented in this study only consider heat advection due to subsurface water flow. However, simple, two-dimensional simulations were also performed to estimate the influence of advection due to surface water flow in the channel fen adjacent to the plateau (supporting information). These calculations indicate that, when the surface water flow is active, this net advective heat transfer is roughly the same order of magnitude as the net heat advection due to groundwater flow. However, the results suggest that on a mean annual basis, the net heat advection due to the surface water

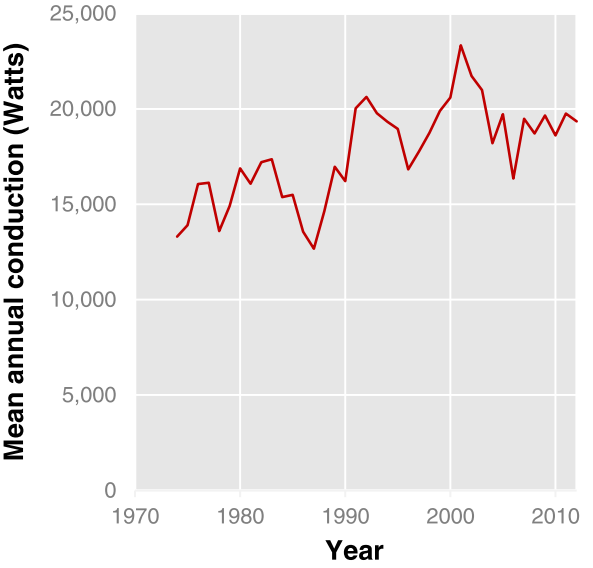

Figure 10. Mean annual conduction entering the model domain through the specified temperature nodes at the upper surface. Results are presented for the moving average of the preceding five years to remove short-term trends.

channel flow is likely less than the net advection due to groundwater flow. In general, the simulated conductive heat flow from the land surface is over an order of magnitude greater than the combined (groundwater and surface water) advective heat transfer during the summer and when averaged out on a mean annual basis.

5.2.3. Landscape Transition and the Positive Climate Change Feedback Effect

The results from this study are also useful for understanding the drivers of landscape transition in subarctic environments. Properly understanding and quantifying processes that cause the shrinking of forested plateaus and the expansion of unforested wetlands is essential for predicting the future loss of boreal forest and associated ecosystems [*Baltzer et al.*, 2014]. The results from this study suggest that the thawing of permafrost bodies and changes to the landscape conditions in discontinuous permafrost regions are mutually interdependent processes. The expansion of wetlands alters the average watershed surface energy balance via the reduction in the forest canopy. As the watershed is increasingly dominated by wetlands, more energy is absorbed at the land surface, and this additional energy can be conducted into the subsurface and produce accelerated permafrost thaw and further landscape transition.

For example, Figure 10 indicates that the simulated mean annual conduction through the top specified surface temperature nodes generally increased from 1970 to 2012. This is partly due to the increase in the wetland surface area and hence average surface temperature. Thus in discontinuous permafrost regions, landscape transition can accelerate permafrost thaw, and permafrost thaw can actuate landscape transition. Given that permafrost thaw and forest loss can both lead to increased atmospheric concentrations of greenhouse gasses [*Schuur et al.*, 2008; *van der Werf et al.*, 2009], these processes act as positive climate change feedback mechanisms. The simulated enhanced permafrost thaw caused by landscape transition helps explain the noted relationship between accelerated thaw rates and increased plateau fragmentation [*Baltzer et al.*, 2014].

5.3. Implications for Future Permafrost Thaw in Colder Environments and Future Modeling Efforts

The permafrost degradation and landscape transition in the Scotty Creek watershed, which is at the forefront of permafrost thaw, provides an interesting case study for the future resilience of permafrost and landscape conditions in colder environments. In particular, the field observations and simulations presented herein suggest that large-scale permafrost thaw will likely occur through the gradual expansion of thawed zones via vertical and lateral heat transfer. The future changes to the hydrologic connectivity induced by landscape transition at these sites may cause pronounced increases to streamflow, such as that experienced in Scotty Creek (Figure 1c). Also, the SUTRA simulations suggest that the shrinking of subplateau permafrost may enhance groundwater flow in near-surface aquifers. These enhanced groundwater flow systems may help to reduce the seasonality of future streamflow. The potential for permafrost thaw to influence groundwater systems and streamflow or to affect ground surface stability has broad implications for oil and gas and mining industries that are continuously expanding northward as well as water resources managers or building designers in cold regions.

The future resilience or sensitivity of permafrost and hydrogeologic regimes in higher latitude environments can be investigated by incorporating the process-oriented modeling sequence presented in this study. Most permafrost models that accommodate complex surface processes, such as vegetation and snowpack, do not simulate lateral subsurface heat transfer [*Riseborough et al.*, 2008]. Conversely, most

numerical models that consider multidimensional heat transfer processes and groundwater flow do not include surface processes [*Kurylyk et al*., 2014a]. The influence of changing climate and land cover conditions on subsurface thermal and hydraulic regimes can be simulated by using climate data to drive surface model simulations for different land cover types, which in turn can form the thermal boundary condition for a numerical model of coupled heat transfer and groundwater flow. To investigate the influence of landscape transition, the subsurface model should be capable of automatically updating the surface boundary condition (i.e., land cover type) based on the presence of absence of permafrost beneath each surface node at the end of the thawing season.

6. Summary and Conclusions

This study has investigated the fundamental drivers of permafrost thaw and landscape transition in the southern limits of the discontinuous permafrost region in the Northwest Territories, Canada. To our knowledge, this is the first study to present results from three-dimensional heat transfer simulations of lowland permafrost thaw informed by field observations. Simulations were performed with and without lateral heat transfer considered, and the differences in the modeling results toward the end of the simulations suggest the importance of lateral subsurface heat transfer in accelerating permafrost degradation in certain environments and timescales. Future modeling efforts in discontinuous permafrost regions should cautiously employ the conventional approach of using models restricted to vertical heat transfer, although the distributed 1-D heat transfer model was shown to perform well for the first third of the simulation. The simulations also indicate that groundwater flow and surface water flow are likely not important heat transfer mechanisms in the study site. However, the simulations demonstrate that, because suprapermafrost groundwater flow is most active during the warm summer months when the temperature difference between the groundwater and permafrost is maximal, groundwater advective heat flux may accelerate permafrost thaw in other catchments with different lithology.

Furthermore, the permafrost distribution was shown to strongly influence the groundwater flow rates. The simulated groundwater flow rate increased from 1970 to 2012 due to the reduction in the hydraulic resistance that the shrinking permafrost body imposed on the local groundwater flow system. The modeling results also emphasize the importance of the positive climate change feedback mechanism caused by the thaw-induced landscape transition from forested peatlands to unforested wetlands. By elucidating the processes governing discontinuous permafrost thaw and related landscape changes, the modeling results have helped to address identified gaps in understanding the sensitivity of discontinuous permafrost to climate warming [*Sjöberg et al*., 2015].

This study only considered heat transfer processes in a particular plateau-wetland complex. The Scotty Creek watershed and the surrounding region are characterized by wetlands intermingled with numerous peat plateaus of various sizes, and discontinuous permafrost regions in Europe and Asia are also characterized by plateau-wetland complexes [e.g., *Sannel et al*., 2015]. The future goal is to upscale the findings of the present study. The permafrost bodies beneath the plateaus have different ratios of permafrost volume, which is an indicator of thermal resistance, to lateral permafrost surface area, which is an indicator of thermal sensitivity. A future study will consider the size distribution of peat plateaus in the region and will investigate how the initial plateau size influences their sensitivity to past and future climate warming.

Appendix A: SUTRA Parameterization

Table A1 lists the thermal and hydraulic parameters, freeze-thaw settings, and numerical solution controls used in SUTRA.

Table A1. Values/Descriptions for the Modeling Parameters in SUTRA

Model Parameter	Value/Description	Notes/Reference
(A) Soil hydraulic properties		
Saturated permeability in peat	Varies	Four scenarios were considered (see Table 1)
Saturated permeability in silty clay	1.0×10^{-16} m^2	Yields a saturated K value of $\sim 6 \times 10^{-10}$ m/s
Peat porosity	0.8	Site conditions, *McClymont et al.* [2013]
Silty clay porosity	0.4	Site conditions, *McClymont et al.* [2013]
(B) Thermal properties		
Peat grain thermal conductivity, λ_s	0.25 W m^{-1}°C^{-1}	*Hillel* [1998]
Silty clay grain therm. cond., λ_s	1.62 W m^{-1}°C^{-1}	*Hillel* [1998]
Peat grain heat capacity, $c_s\rho_s$	2.6×10^6 J m^{-3}°C^{-1}	Inferred from bulk soil heat capacity
Silty clay grain heat capacity, $c_s\rho_s$	2.0×10^6 J m^{-3}°C^{-1}	Inferred from bulk soil heat capacity
Water thermal conductivity, λ_L	0.6 W m^{-1}°C^{-1}	*Bonan* [2008]
Water heat capacity, $\rho_L c_L$	4.18×10^6 J m^{-3}°C^{-1}	*Bonan* [2008]
Ice thermal conductivity, λ_I	2.14 W m^{-1}°C^{-1}	SUTRA value [*Williams and Smith*, 1989]
Ice heat capacity, $\rho_I c_I$	1.94×10^6 J m^{-3}°C^{-1}	*Williams and Smith* [1989]
(C) Soil freezing and relative permeability functions		
Soil freezing curve	Power	*Andersland and Ladanyi* [1994]; equation (4)
Freezing curve, α for peat	0.22	Site conditions, *Zhang et al.* [2008a]
Freezing curve, β for peat	−0.15	Site conditions, *Zhang et al.* [2008a]
Freezing curve, α for silty clay	0.15	Silty clay data, *Tarnawski and Wagner* [1993]
Freezing curve, β for silty clay	−0.4	Silty clay data, *Tarnawski and Wagner* [1993]
Residual liquid sat (S_{wresi})	0.1	Silty clay data, *Tarnawski and Wagner* [1993]
Minimum relative permeability	1E-8	k_{rel} decreases linearly with S_L until $S_L = S_{wresi}$
(D) SUTRA discretization and solver settings		
Finite element mesh type	Regular rectilinear	User-controlled mesh generated in Argus ONE
Element height in peat layer	0.1 to 0.21 m	Element height increases linearly with depth
Element height in silty clay layer	0.5 to 3.5 m	Element height increases linearly with depth
Plan view element dimensions	1 m × 1 m	See comments in text
Number of nodes	376,431	360,000 elements
Constant time step size	1 day	Time step size required due to freezing processes
Number of time steps	15,695	43 years × 365 days per year (1970–2012)
Pressure solution solver	Iterative	IC-preconditioned conjugate gradient
Temperature solution solver	Iterative	ILU-preconditioned generalized min. residual

Acknowledgments

The data presented in this paper can be made available by contacting the authors. Field data collection for this study was funded by the Canadian Space Agency, the Canadian Foundation for Climate and Atmospheric Sciences, Natural Sciences and Engineering Research Council of Canada, and International Polar Year. Yu Zhang (Natural Resources Canada) and Brendan Christensen (Worley Parsons) provided many helpful suggestions related to the NEST modeling. Alex Cannon (Pacific Climate Impacts Consortium) was helpful in obtaining the climate scenarios that were ultimately used as the basis for the simple linear warming scenarios applied in this study. Ryan Connon (Wilfrid Laurier University) provided helpful discussions related to the study site. Helpful comments from the Editor, Jean Bahr, the Associate Editor, three anonymous reviewers, and Michelle Walvoord (USGS) improved the quality of this paper. We also wish to sincerely thank the Dehcho First Nations, in particular the Liidlii Kue First Nation and the Jean-Marie River First Nation, for their support of the Scotty Creek research station. B. Kurylyk was funded from postdoctoral fellowships from the Killam Trust, the Natural Sciences and Engineering Research Council of Canada, and the University of Calgary Eyes High Program.

References

Andersland, O. B., and B. Ladanyi (1994), *An Introduction to Frozen Ground Engineering*, Chapman and Hall, N. Y.

Anderson, M. P. (2005), Heat as a ground water tracer, *Groundwater*, *43*, 951–968, doi:10.1111/j.1745-6584.2005.00052.x.

Baltzer, J. L., T. Veness, L. E. Chasmer, A. E. Sniderhan, and W. L. Quinton (2014), Forests on thawing permafrost: Fragmentation, edge effects, and net forest loss, *Global Change Biol.*, *20*(3), 824–834, doi:10.1111/gcb.12349.

Bear, J. (1972), *Dynamics of Fluids in Porous Media*, Elsevier, N. Y.

Bense, V. F., G. Ferguson, and H. Kooi (2009), Evolution of shallow groundwater flow systems in areas of degrading permafrost, *Geophys. Res. Lett.*, *36*, L22401, doi:10.1029/2009GL039225.

Bense, V. F., H. Kooi, G. Ferguson, and T. Read (2012), Permafrost degradation as a control on hydrogeological regime shifts in a warming climate, *J. Geophys. Res.*, *117*, F030363, doi:10.1029/2011JF002143.

Blackwell, D., and M. Richards (2004), Geothermal map of North America, Map 423, scale 1:6,500,000, Am. Assoc. of Pet. Geol., Davis, Calif.

Bonan, G. (2008), *Ecological Climatology*, Cambridge Univ. Press, Cambridge, U. K.

Briggs, M. A., M. A. Walvoord, J. M. McKenzie, C. I. Voss, F. D. Day-Lewis, and J. W. Lane (2014), New permafrost is forming around shrinking Arctic lakes, but will it last?, *Geophys. Res. Lett.*, *41*, 1585–1592, doi:10.1002/2014GL059251.

Bristow, K. L., and G. S. Campbell (1984), On the relationship between incoming solar radiation and daily maximum and minimum temperature, *Agric. Forest Meteorol.*, *31*(2), 159–166, doi:10.1016/0168-1923(84)90017-0.

Carey, S. K., and M.-K. Woo (2005), Freezing of subarctic hillslopes, Wolf Creek basin, Yukon, Canada, *Arct. Antarct. Alp. Res.*, *37*(1), 1–10, doi:10.1657/1523-0430(2005)037[0001:FOSHWC]2.0.CO;2.

Cheng, G., and H. Jin (2013), Permafrost and groundwater on the Qinghai-Tibet plateau, *Hydrogeol. J.*, *21*(1), 5–23, doi:10.1007/s10040-012-0927-2.

Christensen, B. S. (2014), Permafrost development and active-layer hydrology of peat plateaus in wetland-dominated discontinuous permafrost, MSc thesis, Dep. of Geosci., Univ. of Calgary, Calgary, Alberta, Canada.

Connon, R.F., W. L. Quinton, J. R. Craig, and M. Hayashi (2014), Changing hydrologic connectivity due to permafrost thaw in the lower Liard River valley, NWT, Canada, *Hydrol. Processes*, *28*(14), 4163–4178, doi:10.1002/hyp.10206.

Constantz, J., M. H. Cox, and G. W. Su (2003), Comparison of heat and bromide as ground water tracers near streams, *Ground Water*, *41*, 647–656.

de Marsily, G. (1986), *Quantitative Hydrogeology*, Academic, San Diego, Calif.

Environment Canada (2013), *Adjusted and Homogenized Canadian Climate Data,* Ottawa, Ontario. [Available at http://www.ec.gc.ca/dccha-ahccd/, accessed on 17 June 2016.]

Environment Canada (2015), *Historical Canadian Climate Data, Environment Canada,* Ottawa, Ontario. [Available at http://climate.weather.gc.ca/index_e.html, accessed on 1 Dec. 2015.]

Frampton, A., S. L. Painter, and G. Destouni (2013), Permafrost degradation and subsurface-flow changes caused by surface warming trends, *Hydrogeol. J.*, *21*(1), 271–280, doi:10.1007/s10040-012-0938-z.
Freeze, R. A., and J. A. Cherry (1973), *Groundwater*, Prentice Hall, Englewood Cliffs, N. J.
Ge, S., J. M. McKenzie, C. I. Voss, and Q. Wu (2011), Exchange of groundwater and surface-water mediated by permafrost response to seasonal and long term air temperature variation, *Geophys. Res. Lett.*, *38*, L14402, doi:10.1029/2011GL047911.
Green, D., R. Perry, and R. Babcock (1964), Longitudinal dispersion of thermal energy through porous media with a flowing fluid, *AIChE J.*,*10*(5), 645–651.
Hayashi, M., W. L. Quinton, A. Pietroniro, and J. J. Gibson (2004), Hydrologic functions of wetlands in a discontinuous permafrost basin indicated by isotopic and chemical signatures, *J. Hydrol.*, *296*(1–4), 81–97, doi:10.1016/j.jhydrol.2004.03.020.
Hayashi, M., N. Goeller, W. L. Quinton, and N. Wright (2007), A simple heat-conduction method for simulating the frost-table depth in hydrological models, *Hydrol. Processes*, *21*(19), 2610–2622, doi:10.1002/hyp.6792.
Hillel, D. (1998), *Environmental Soil Physics*, Academic, San Diego, Calif.
Hopmans, J. W., J. Simunek, and K. L. Bristow (2002), Indirect estimation of soil thermal properties and water flux using heat pulse probe measurements: Geometry and dispersion effects, *Water Resour. Res.*, *38*(1), 1006, doi:10.1029/2000WR000071.
Huber, M. L., R. A. Perkins, A. Laesecke, D. G. Friend, J. V. Sengers, M. J. Assael, I. N. Metaxa, E. Vogel, R. Mares, and K. Miyagawa (2009), New international formulation for the viscosity of H_20, *J. Phys. Chem. Ref. Data Monogr.*, *38*(2), 101–125, doi:10.1063/1.3088050.
Ingebritsen, S. E., and W. E. Sanford (1998), *Groundwater in Geologic Processes*, Cambridge Univ. Press, Cambridge, U. K.
Johannessen, O. M., et al. (2004), Arctic climate change: Observed and modelled temperature and sea-ice variability, *Tellus Ser. A*, *56*(4), 328–341, doi:10.1111/j.1600-0870.2004.00060.x.
Jury, W. A., and R. Horton (2004), *Soil Physics*, 6th ed., John Wiley, Hoboken, N. J.
Kane, D. L., L. D. Hinzman, and J. P. Zarling (1991), Thermal response of the active layer to climatic warming in a permafrost environment, *Cold Reg. Sci. Technol.*, *19*(2), 111–122, doi:10.1016/0165-232X(91)90002-X.
Kane, D. L., K. Yoshikawa, and J. P. McNamara (2013), Regional groundwater flow in an area mapped as continuous permafrost, NE Alaska (USA), *Hydrogeol. J.*, *21*(1), 41–52, doi:10.1007/s10040-012-0937-0.
Kurylyk, B. L., and K. Watanabe (2013), The mathematical representation of freezing and thawing processes in variably-saturated, non-deformable soils, *Adv. Wat. Resour.*, *60*, 160–177, doi:10.1016/j.advwatres.2013.07.01.
Kurylyk, B. L., K. T. B. MacQuarrie, and J. M. McKenzie (2014a), Climate change impacts on groundwater and soil temperatures in cold and temperate regions: Implications, mathematical theory, and emerging simulation tools, *Earth Sci. Rev.*, *138*, 313–334, doi:10.1016/j.earscirev.2014.06.006.
Kurylyk, B. L., K. T. B. MacQuarrie, and C. I. Voss (2014b), Climate change impacts on the temperature and magnitude of groundwater discharge from shallow, unconfined aquifers, *Water Resour. Res.*, *50*, 3253–3274, doi:10.1002/2013WR014588.
Kurylyk, B. L., R. D. Moore, and K. T. B. MacQuarrie (2015), Scientific briefing: Quantifying streambed heat advection associated with groundwater-surface water interactions, *Hydrol. Processes*, doi:10.1002/hyp.10709, in press.
Lunardini, V. J. (1981), *Heat Transfer in Cold Climates*, van Nostrand Reinhold, N. Y.
McClymont, A. F., M. Hayashi, L. R. Bentley, and B. S. Christensen (2013), Geophysical imaging and thermal modeling of subsurface morphology and thaw evolution of discontinuous permafrost, *J. Geophys. Res. Earth Surf.*, *118*, 1826–1837, doi:10.1002/jgrf.20114.
McKenzie, J. M., and C. I. Voss (2013), Permafrost thaw in a nested groundwater-flow system, *Hydrogeol. J.*, *21*(1), 299–316, doi:10.1007/s10040-012-0942-3.
McKenzie, J. M., C. I. Voss, and D. I. Siegel (2007a), Groundwater flow with energy transport and water–ice phase change: Numerical simulations, benchmarks, and application to freezing in peat bogs, *Adv. Wat. Resour.*, *30*, 966–983, doi:10.1016/j.advwatres.2006.08.008.
McKenzie, J. M., D. I. Siegel, D. O. Rosenberry, P. H. Glaser, and C. I. Voss (2007b), Heat transport in the Red Lake Bog, Glacial Lake Agassiz Peatlands, *Hydrol. Processes*, *21*(3), 369–378, doi:10.1002/hyp.6239.
Metcalfe, R. A., and J. M. Buttle (1999), Semi-distributed water balance dynamics in a small boreal forest basin, *J. Hydrol.*, *226*(1–2), 66–87, doi:10.1016/S0022-1694(99)00156-0.
Metzger, T., S. Didierjean, and D. Maillet (2004), Optimal experimental estimation of thermal dispersion coefficients in porous media. *Int. J. Heat Mass Transfer*, *47*(14–16), 3341–3353, doi:10.1016/j.ijheatmasstransfer.2004.02.024.
Nagare, R. M., R. A. Schincariol, W. L. Quinton, and M. Hayashi (2012), Moving the field into the lab: Simulation of water and heat transport in subarctic peat, *Permafr. Periglac. Process.*, *23*(3), 237–243, doi:10.1002/ppp.1746.
Nelson, F. E., N. I. Shiklomanov, G. R. Mueller, K. M. Hinkel, D. A. Walker, and J. G. Bockheim (1997), Estimating active-layer thickness over a large region: Kuparuk River Basin, Alaska, USA, *Arct. Antarct. Alp. Res.*, *29*(4), 367–378, doi:10.2307/1551985.
Noetzli, J., and S. Gruber (2009), Transient thermal affects in Alpine permafrost, *The Cryosphere*, *3*, 85–99, doi:10.5194/tc-3-85-2009.
Noetzli, J., S. Gruber, T. Kohl, N. Salzmann, and W. W. Haeberli (2007), Three-dimensional distribution and evolution of permafrost temperatures in idealized high-mountain topography, *J. Geophys. Res.*, *112*, F02S13, doi:10.1029/2006JF000545.
Pang, Q, L. Zhao, S. Li, and Y. Ding (2012), Active layer thickness variations on the Qinghai-Tibet Plateau under the scenarios of climate change, *Environ. Earth Sci.*, *66*(3), 849–857, doi:10.1007/s12665-011-1296-1.
Pacific Climate Impacts Consortium (2014), Statistically downscaled climate scenarios. [Available at http://www.pacificclimate.org/data/statistically-downscaled-climate-scenarios, last accessed on 20 Oct. 2014.]
Quinton, W. L., and P. Marsh (1999), A conceptual framework for runoff generation in a permafrost environment, *Hydrol. Processes*, *13*(16), 2563–2581, doi:10.1002/(SICI)1099-1085(199911)13:16 < 2563::AID-HYP942 > 3.0.CO;2-D.
Quinton, W. L., M. Hayashi, and A. Pietroniro (2003), Connectivity and storage functions of channel fens and flat bogs in northern basins, *Hydrol. Processes*, *17*(18), 3665–3684, doi:10.1002/hyp.1369.
Quinton, W. L., M. Hayashi, and S. K. Carey (2008), Peat hydraulic conductivity in cold regions and its relation to pore size and geometry, *Hydrol. Processes*, *22*(15), 2829–2837, doi:10.1002/hyp.7027.
Quinton, W. L., M. Hayashi, and L. E. Chasmer (2011), Permafrost-thaw-induced land-cover change in the Canadian subarctic: Implications for water resources, *Hydrol. Processes*, *25*(1), 152–158, doi:10.1002/hyp.7894.
Rau, G. C., M. S. Andersen, and R. I. Acworth (2012) Experimental investigation of the thermal dispersivity term and its significance in the heat transport equation for flow in sediments, *Water Resour. Res.*, *48*, W03511, doi:10.1029/2011WR011038.
Riseborough, D., N. Shiklomanov, B. Etzelmüller, S. Gruber, and S. Marchenko (2008), Recent advances in permafrost modelling, *Permafr. Periglac. Process.*, *19*(2), 137–156, doi:10.1002/ppp.615.
Running, S.W., R. R. Nemani, and R. D. Hungerford (1987), Extrapolation of synoptic meteorological data in mountainous terrain and its use for simulating forest evapotranspiration and photosynthesis, *Can. J. For. Res.*, *17*(6), 472–483, doi:10.1139/x87-081.

Sannel, A. B. K., G. Hugelius, P. Jansson, and P. Kuhry (2015), Permafrost warming in a subarctic peatland: Which meteorological controls are most important?, *Permafr. Periglac. Process.*, doi:10.1002/ppp.1862, in press.
Sauty, J. P., A. C. Gringarten, A. Menjoz, and P. A. Landel (1982), Sensible energy storage in aquifers 1. Theoretical study, *Water Resour. Res.*, *18*, 245–252.
Scheidegger, J. M., and V. F. Bense (2014), Impacts of glacially recharged groundwater flow systems on TALIK evolution, *J. Geophys. Res. Earth Surf.*, *119*, 758–778, doi:10.1002/2013JF002894.
Schuur, E. A. G., et al. (2008), Vulnerability of permafrost carbon to climate change: Implications for the global carbon cycle, *Bioscience*, *58*(8), 701–714, doi:10.1641/B580807.
Sjöberg, Y., A. Frampton, and S. W. Lyon (2013), Using streamflow characteristics to explore permafrost thawing in northern Swedish catchments, *Hydrogeol. J.*, *21*(1), 121–131, doi:10.1007/s10040-012-0932-5.
Sjöberg Y., E. Coon, A. B. K. Sannel, R. Pannetier, D. Harp, A. Frampton, S. L. Painter, and S. W. Lyon (2016), Thermal effects of groundwater flow through subarctic fens-A case study based on field observations and numerical modeling, *Water Resour, Res.*, doi:10.1002/2015WR017571, in press.
Sjöberg, Y., P. Marklund, R. Pettersson, and S. W. Lyon (2015), Geophysical mapping of palsa peatland permafrost, *Cryosphere*, *9*, 465–478, doi:10.5194/tc-9-465-2015.
Smith, L., and D. S. Chapman (1983), On the thermal effects of groundwater flow 1. Regional scale systems, *J. Geophys. Res.*, *88*, 593–608.
Smith, M. W., and D. W. Riseborough (2002), Climate and the limits of permafrost: A zonal analysis, *Permafr. Periglac. Process.*, *13*(1), 1–15, doi:10.1002/ppp.410.
Smith, S. L., and D. W. Riseborough (2010), Modelling the thermal response of permafrost terrain to right-of-way disturbance and climate warming, *Cold Reg. Sci. Technol.*, *60*(1), 92–103, doi:10.1016/j.coldregions.2009.08.009.
Spence, C., and M.-K. Woo (2003), Hydrology of subarctic Canadian Shield: Soil-filled valleys, *J. Hydrol.*, *279*(1–4), 151–166, doi:10.1016/S0022-1694(03)00175-6.
Stähli, M. (2005), Freezing and thawing phenomena in soils, in *Encyclopedia of the Hydrological Sciences*, edited by M. G. Anderson, pp. 1069–1076, John Wiley, Hoboken, N. J.
St. Jacques, J.-M, and D. J. Sauchyn (2009), Increasing winter baseflow and mean annual streamflow from possible permafrost thawing in the Northwest Territories, Canada, *Geophys. Res. Lett.*, *36*, L01401, doi:10.1029/2008GL035822.
Szeicz, J. M., and G. M. MacDonald (1995), Dendroclimatic reconstruction of summer temperatures in Northwestern Canada since A.D. 1638 based on age-dependent modeling, *Quat. Res.*, *44*(2), 257–266, doi:10.1006/qres.1995.1070.
Tarnawski, V. R., and B. Wagner (1993), Modeling the thermal conductivity of frozen soils, *Cold Reg. Sci. Technol.*, *22*(1), 19–31, doi:10.1016/0165-232X(93)90043-8.
Voss C. I., and A. M. Provost (2010), SUTRA: A Model for Saturated-Unsaturated Variable-Density Ground-Water Flow with Solute or Energy Transport, *Water Invest. Rep. 02-4231*, U.S. Geol. Survey, Reston, Va.
van der Werf, G. R., D. C. Morton, R. S. DeFries, J. G. J. Olivier, P. S. Kasibhatla, R. B. Jackson, G. J. Collatz, and J. T. Randerson (2009), CO_2 emissions from forest loss, *Nat. Geosci.*, *2*, 737–738, doi:10.1038/ngeo671.
van Vuuren D. P., et al. (2011), The representative concentration pathways: An overview, *Clim. Change*, *109*(1–2), 5–31, doi:10.1007/s10584-011-0148-z.
Walvoord, M. A., and R. G. Striegl (2007), Increased groundwater to stream discharge from permafrost thawing in the Yukon River basin: Potential impacts on lateral export of carbon and nitrogen, *Geophys. Res. Lett.*, *34*, L12402, doi:10.1029/2007GL030216.
Walvoord, M. A., C. I. Voss, and T. P. Wellman (2012), Influence of permafrost distribution on groundwater flow in the context of climate-driven permafrost thaw: Example from Yukon Flats Basin, Alaska, United States, *Water Resour. Res.*, *48*, W07524, doi:10.10129/2011WR011595.
Watanabe, K, and M. Flury (2008), Capillary bundle model of hydraulic conductivity for frozen soil, *Water Resour. Res.*, *44*, W12402, doi:10.1029/2008WR007012.
Wellman, T. P., C. I. Voss, and M. A. Walvoord (2013), Impacts of climate, lake size, and supra- and sub-permafrost groundwater flow on lake-talik evolution, Yukon Flats, Alaska (USA), *Hydrogeol. J.*, *21*(1), 281–298, doi:10.1007/s10040-012-0941-4.
Williams, P. J., and M. W. Smith (1989), *The Frozen Earth: Fundamentals of Geocryology*, Cambridge University Press, Cambridge, U. K.
Woo, M.-K. (2012), *Permafrost Hydrology*, Springer, Berlin.
Woo, M.-K, D. L. Kane, S. K. Carey, and D. Yang (2008), Progress in permafrost hydrology in the new millennium, *Permafr. Periglac. Process.*, *19*(2), 237–254, doi:10.1002/ppp.613.
Wright, N., W. L. Quinton, and M. Hayashi (2008), Hillslope runoff from an ice-cored peat plateau in a discontinuous permafrost basin, Northwest Territories, Canada, *Hydrol. Processes*, *22*(15), 2816–2828, doi:10.1002/hyp.7005.
Wright, N., M. Hayashi, W. L. Quinton (2009), Spatial and temporal variations in active layer thawing and their implication on runoff generation in peat-covered permafrost terrain, *Water Resour. Res.*, *45*, W05414, doi:10.1029/2008WR006880.
Zhang, Y., W. J. Chen, and J. Cihlar (2003), A process-based model for quantifying the impact of climate change on permafrost thermal regimes, *J. Geophys. Res.*, *108*(D22), 4695, doi:10.1029/2002JD003354.
Zhang, Y., S. K. Carey, and W. L. Quinton (2008a), Evaluation of the algorithms and parameterizations for ground thawing and freezing simulation in permafrost regions, *J. Geophys. Res.*, *113*, D17116, doi:10.1029/2007JD009343.
Zhang, Y., W. Chen, and D. W. Riseborough (2008b), Disequilibrium response of permafrost thaw to climate warming in Canada over 1850-2100, *Geophys. Res. Lett.*, *35*, L02502, doi:10.1029/2007GL032117.
Zhang, Y., J. Li, X. Wang, W. Chen, W. Sladen, I. Dyke, L. Dredge, J. Poitevin, D. McLennan, H. Stewart, S. Kowalchuk, W. Wu, G. P. Kershaw, and R. K. Brook (2012), Modelling and mapping permafrost at high spatial resolution in Wapusk National Park, Hudson Bay Lowlands, *Can. J. Earth Sci.*, *49*(8), 925–937, doi:10.1139/e2012-031.